# Molecular Dynamics Study of the Influence of Solid Interfaces on Poly(ethylene oxide) Structure and Dynamics

**Oleg Borodin,*,† Grant D. Smith,†,‡ Rajdip Bandyopadhyaya,§ and Oleksiy Byutner†**

*Department of Materials Science and Engineering, 122 S. Central Campus Drive, Rm. 304, and Department of Chemical and Fuels Engineering, University of Utah, Salt Lake City, Utah 84112*

*Received May 9, 2003; Revised Manuscript Received August 6, 2003*

ABSTRACT: Molecular dynamics (MD) simulation studies of the interface between poly(ethylene oxide) (PEO) and $TiO_2$ have been performed at 423 K using a quantum chemistry-based force field. MD simulations revealed that the PEO density is significantly perturbed by $TiO_2$ surfaces, forming layers of highly dense polymer (compared to the bulk melt) that persisted up to 15 Å from the surface. Conformational and structural relaxations of the interfacial PEO were found to be dramatically slower than those of bulk PEO. These effects are attributed to an intrinsic slowing down of PEO dynamics and increased dynamic heterogeneity of the interfacial polymer. The surface structure and electrostatic interactions between PEO and $TiO_2$, rather than the increased polymer density at the $TiO_2$ surface, determine the nature of PEO relaxation at the $TiO_2$ interface.

## I. Introduction

The addition of nanoparticles to polymers allows one to alter the structural and mechanical properties of the polymer matrix while keeping the chemical properties of the polymer intact. The dramatic changes in the polymer glass-transition temperature, the appearance of a second glass-transition temperature at a certain range of filler volume fraction,[1,2] changes in dynamic−mechanical properties,[2] dielectric relaxation,[3] and polymer dynamics[4,5] observed for numerous polymer nanocomposites and thin films open a realm of possibilities for the modification of polymer properties by the addition of nanoparticles.[6,7] The potential impact of modification of polymer properties at interfaces also has significant ramifications on the design of new lubricants,[8] adhesives, polymer electrolytes,[9] protective coating,[10] and photolithography, inspiring numerous theoretical and experimental efforts directed toward gaining a fundamental understanding of polymer-filled systems.

The influence of nanoparticles on the dynamic−mechanical properties of polymers was investigated by Tsagaropoulos and Eisenberg in dynamic−mechanical and thermal analysis studies.[1,2] Poly(dimethylsiloxane) and poly(vinyl acetate) polymers filled with silica nanoparticles exhibited the appearance of the second glass-transition temperature at a sufficiently high volume fraction of silica nanoparticles.[2] This (second) glass transition occurred at a higher temperature than the glass transition of the pure matrix polymer and was associated with the dynamics of the polymer loosely bound to nanoparticles, whereas the lower glass-transition temperature was associated with the dynamics of the bulk polymer. The nature of the nanoparticle−polymer interactions and the volume fraction of nanoparticles were found to have a significant influence on the higher glass-transition temperature and almost no effect on the glass transition at lower temperature. The elastic modulus of poly(ethylene oxide) (PEO)/$SiO_2$ nanocomposites was found in a separate study[11] to be strongly dependent on the surface modification of $SiO_2$ nanoparticles, indicating the importance of PEO−nanoparticle interactions on nanocomposite mechanical properties.

Coarse-grained molecular dynamics (MD)[12−17] and Monte Carlo[18−20] simulations have provided valuable insight into factors responsible for altering polymer matrix properties with the addition of interfaces. The strength of the nanoparticle−polymer interaction and the nanoparticle specific surface area were found to be the most important factors controlling the properties of the interfacial polymer. The addition of nanoparticles with attractive interactions led to decreased polymer dynamics and increased viscosity, whereas the addition of nanoparticles with the repulsive, or excluded volume, interactions led to increased polymer dynamics and decreased viscosity.[15,16] These effects were found to scale linearly with the specific surface area of nanoparticles.[15] Another important factor controlling interfacial polymer dynamics is the structure of the surface.[13,21] The polymers next to the structureless, or flat, surfaces with the attractive surface−polymer interactions were found to exhibit quite different dynamics than polymers near structured surfaces. In the later case, polymer motion near the surface was found to be strongly correlated to the surface structure.[21]

We are interested in understanding the influence of the strength of the (PEO) interactions with $TiO_2$ surfaces and the effect of the $TiO_2$ surface structure on PEO structural, conformational, and dynamic properties near $TiO_2$ surfaces. The PEO/$TiO_2$ system has been chosen because PEO is a major component of PEO-based solid polymer electrolytes, which are potential candidates for use in solvent-free secondary lithium batteries. The addition of ceramic nanoparticles to polymer electrolytes, initially done to enhance mechanical properties, has also been found to improve the anodic stability,[22] cyclability,[23,24] sometimes conductivity,[22,25−27] and cation transfer number[22,25,26] of polymer electrolytes without

* Corresponding author. E-mail: Oleg.Borodin@utah.edu.
† Department of Materials Science and Engineering.
‡ Department of Chemical and Fuels Engineering.
§ Present address: Department of Chemical Engineering, University of California, Los Angeles, California 90095-1592.

10.1021/ma0346005 CCC: $25.00 
Published on Web 09/12/2003

causing any observed degradations. A fundamental understanding of the mechanisms responsible for the dramatic changes in polymer electrolyte properties with the addition of nanoparticles is lacking. This MD simulation study of the PEO/$TiO_2$ system is the first step toward understanding more complicated PEO/Li salt/$TiO_2$ systems.

This paper is organized in the following order. In section II, the development of the quantum chemistry-based force field for the PEO/$TiO_2$ interactions is presented. In section III, MD simulations methodology is described together with the simulated systems. The results of MD simulations of PEO sandwiched between $TiO_2$ surfaces are presented and discussed in section IV. Then we investigate in section V the influence of the surface structure on the interfacial PEO dynamics and structure by performing simulations of PEO near flat, or structureless, surfaces having the same PEO density profile normal to the surface as observed in the PEO/$TiO_2$ system. The influence of the strength of the surface−polymer interaction of PEO dynamics is studied in section VI.

## II. Force Field Development.

**A. Energetics of $TiO_5H_9$−Dimethyl Ether Complexation.** An accurate prediction of the strength of the PEO−$TiO_2$ interactions is important for a realistic representation of the PEO structural and dynamic properties in the proximity of $TiO_2$ surfaces. Because accurate quantum chemistry calculations of high molecular weight PEO next to $TiO_2$ surfaces are prohibitively expensive, we studied the PEO−$TiO_2$ interactions using a representative model system consisting of a PEO monomer (dimethyl ether) complexed with the $TiO_5H_9$ cluster, as illustrated in Figure 1. Then the PEO−$TiO_2$ force field was developed upon the basis of $TiO_5H_9$−dimethyl ether energetics and was used in MD simulations of PEO−$TiO_2$.

All quantum chemistry calculations have been performed with the Gaussian 98 package.[28] The binding energy is defined as the energy of the dimethyl ether/$TiO_5H_9$ complex minus the energies of the isolated dimethyl ether and $TiO_5H_9$ using cluster geometries. Binding energies were calculated along the two $C_s$ symmetry paths shown in Figure 1 at the Hartree−Fock (HF) level and using Møller−Plesset second-order perturbation theory (MP2) with the basis sets described below. The geometry of the $TiO_5H_9$ cluster was frozen to that of the anatase crystal. Hydrogen atoms were added to the $TiO_5$ cluster along the directions of the O−Ti bonds in the $TiO_2$ crystal. The O−H bond length was fixed to 0.97 Å. The MP2/aug-cc-pvTz geometry was used for dimethyl ether. The binding energies were corrected for basis set superposition error using the counterpoise method.[29] Three basis sets were employed in the study: (a) 6-31G* for all atoms (170 basis functions), yielding a BSSE-corrected MP2 binding energy of −8.3 kcal/mol; (b) 6-311+G(3f2g) for Ti and aug-cc-pvDz[30] for O, C, and H (326 basis functions), yielding a binding energy of −10.8 kcal/mol; and (c) 6-311+G(3f2g) for Ti and aug-cc-pvTz for O, C, and H (736 basis functions), yielding a binding energy of −11.5 kcal/mol. The dimethyl ether/$TiO_5H_9$ binding energy calculated at the MP2/6-31G* level (−8.3 kcal/mol) is much lower than the binding energies of −10.8 and −11.5 kcal/mol calculated at the MP2 level using much larger basis sets aug-cc-pvDz and aug-cc-pvTz for C, O, and H, respectively, and the 6-311+G(3f2g) basis set for Ti, indicating that the 6-31G* basis set yields inaccurate predictions of the dimethyl ether/$TiO_5H_9$ binding energies. Using the aug-cc-pvTz basis set for the C, O, and H atoms, however, is very expensive and yielded a dimethyl ether/$TiO_5H_9$ binding energy close to that calculated at the MP2/(6-311+G(3f2g) level for Ti and the aug-cc-pvDz level for C, O, and H; therefore, we suggest that the most optimal way of calculating the dimethyl ether/$TiO_5H_9$ binding energy along paths 1 and 2 from Figure 1 is to perform calculations using the intermediate-sized basis set (6-311+G(3f2g) for Ti, aug-cc-pvDz) at the MP2 level and scale them by a factor of 1.07. This factor is the ratio of the dimethyl ether/$TiO_5H_9$ binding energies (MP2/(6-311+G(3f2g) for Ti, aug-cc-pvTz for C, O, H) and MP2/(6-311+G(3f2g) for Ti, and aug-cc-pvDz for C, O, H) calculated at the geometry corresponding to the minimum energy along path 1.

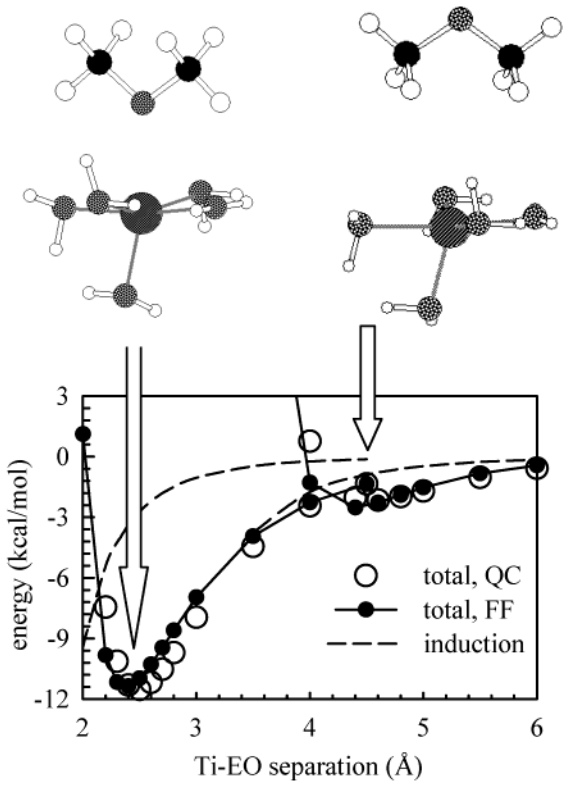


**Figure 1.** BSSE-corrected binding energy for the $CH_3OCH_3$/$TiO_5H_9$ complex calculated at the MP2/6-311+G(3f2g) level for Ti and at the aug-cc-pvDz level and from the force field. The many-body polarization (induction) energy estimate from the force field is also shown.

**B. Force Field Parametrization.** A force field of the form

$$U^{\mathrm{NB}}(\mathbf{r}) = \frac{1}{2}\left[\sum_i \sum_j A_{ij} \exp(-B_{ij} r_{ij}) + \frac{A'_{ij}}{r_{ij}^{12}} - \frac{C_{ij}}{r_{ij}^{6}} + \frac{q_i q_j}{4\pi\epsilon_0 r_{ij}}\right] + U^{\mathrm{pol}}(\mathbf{r}) \quad (1)$$

was parametrized to reproduce the binding energy of the dimethyl ether/$TiO_5H_9$ cluster. Either the exp-6 ($A_{ij}$ exp($B_{ij}r_{ij}$)) or Lennard-Jones 12's power ($A'_{ij}/r_{ij}^{12}$) was used to represent atom−atom repulsion. The potential energy due to dipole polarization $U^{\mathrm{pol}}(\mathbf{r})$ is not pairwise

**Table 1. Partial Charges of Titanium Oxide Clusters from Fits to the Electrostatic Potential around the Titanium Oxide Clusters from ab Initio Quantum Chemistry Calculations[a]**

| | | | partial charges (e) | | | |
|---|---|---|---|---|---|---|
| complex | level of theory | basis set | Ti | O(no H) | O(OH) | O(H2O) |
| $TiO_5H_9$ | MP2 | O-Dz/Ti-6-311+G(3f2g) | 1.292 | | −0.661 | −0.744 |
| $TiO_5H_9$ | MP2 | 6-31G* | 1.377 | | −0.757 | −0.741 |
| $TiO_5H_9$ | HF | 6-31G* | 1.774 | | −0.855 | −0.862 |
| $Ti_2O_9H_{10}$ | MP2 | O-Dz/Ti-6-311+G(3f2g) | 1.247 | −0.68 | −0.678 | −0.658 |
| $Ti_2O_9H_{10}$ | MP2 | 6-31G* | 1.37 | −0.773 | −0.767 | −0.697 |
| $Ti_2O_9H_{10}$ | HF | 6-31G* | 1.669 | −0.865 | −0.868 | −0.764 |

[a] The aug-cc-pvDz basis set is denoted Dz.

additive and is given by the sum of the interaction energy between the induced dipoles ($\boldsymbol{\mu}_i$) and the electric field $\mathbf{E}_i^0$ at atom $i$ generated by the partial charges in the system (first term in eq 2), the interaction energy between the induced dipoles (second term in eq 2), and the energy required to induce the dipole moments $\boldsymbol{\mu}_i$ (third term in eq 2):[31]

$$U^{\mathrm{pol}}(\mathbf{r}) = -\sum_i \boldsymbol{\mu}_i \cdot \mathbf{E}_i^0 - 0.5\sum_i \sum_j \boldsymbol{\mu}_i \cdot \mathbf{T}_{ij} \cdot \boldsymbol{\mu}_j + \sum_i \left( \frac{\boldsymbol{\mu}_i \cdot \boldsymbol{\mu}_i}{2\alpha_i} \right) \quad (2)$$

where $\boldsymbol{\mu}_i = \alpha_i \mathbf{E}_{\mathrm{tot}}$, $\alpha_i$ is the isotropic atomic dipole polarizability, $\mathbf{E}_{\mathrm{tot}}$ is the total electrostatic field at atomic site $i$ due to permanent charges and induced dipoles, and $\mathbf{T}_{ij}$ is the second-order dipole tensor.[32] The nonbonded contributions including the potential energy due to polarization were calculated for all intermolecular dimethyl ether/$TiO_2$ atom pairs ($ij$) and for the intramolecular atom pairs separated by more than two bonds for dimethyl ether.

Partial charges, geometries, and polarizabilities of dimethyl ether and PEO have been previously obtained,[33] leaving only partial charges, polarizabilities of $TiO_2$ and (Ti,O)/PEO exp-6, or Lennard-Jones parameters to be determined. We proceeded with the $TiO_2$/PEO force field parametrization in the following order: in the first step, the Ti and $O_{Ti}$ dipole polarizabilities were determined (the $O_{Ti}$ symbol denotes the oxygen belonging to the $TiO_2$ complex (or surface), which is not to be confused with the ether oxygen); in the second step, the Ti and $O_{Ti}$ partial charges were found; in the third step, the (Ti,$O_{Ti}$)/PEO exp-6 and Lennard-Jones parameters were fit to the $CH_3OCH_3/TiO_5H_9$ binding energies along paths 1 and 2 shown in Figure 1; and in the fourth step, the two-body approximation to the many-body force field was developed.

We determine atom polarizabilities by fitting the polarization energy around a cluster or a molecule found from quantum chemistry calculations. The polarization energy around the $TiO_5H_9$ cluster due to a unit charge (+1e) was calculated along path 1 of Figure 1 in the following way: First, the total energy of the unit charge complexed with the $TiO_5H_9$ cluster is calculated at the HF/(6-311+G(3f2g) level for Ti and the aug-cc-pvTz level for O and H. Then the energy of the $TiO_5H_9$ cluster and the electrostatic potential at the point of the unit charge, calculated at the same level, are subtracted from the total energy of the unit charge−$TiO_5H_9$ cluster, yielding the polarization energy along path 1. Atomic dipole polarizabilities of Ti and O of 0.7 and 1.3 Å$^3$, respectively, were found from the fit of the polarization energy along path 1 from the force field (eq 2) to the polarization energy from quantum chemistry calculations. The polarizability of hydrogen atoms was assumed to be zero during the fit.

Partial charges of Ti, $O_{Ti}$, and $H_{Ti}$ were obtained by fitting the electrostatic grid around the $Ti_xO_yH_z$ clusters. Following Breneman et al.,[34] we excluded the electrostatic potential grid points inside the atomic VDW radii from the fit because the approach of any atom inside the VDW radii of another atom is highly unlikely in MD simulations. The following VDW radii were used: 1.8 Å for H, 1.9 Å for O, and 2.2 Å for Ti. Electrostatic grid points farther than 3.5 Å from any atom were also excluded from the fit in order to obtain relatively homogeneous layers of electrostatic grid points around the cluster. The resulting partial charges for Ti and $O_{Ti}$ are given in Table 1. This Table indicates that a small 6-31G* basis set and the HF level of theory yielded the Ti partial charge of (1.77−1.67e), which is much higher than the Ti partial charges obtained from the fits to the electrostatic potential at the most accurate level investigated (MP2/(6-311+G(3f2 g) for Ti and aug-cc-pvTz for O and H), which in turn yielded a Ti partial charge of around 1.25−1.3e. A similar tendency is seen for the oxygen partial charge. The fits to the electrostatic grid calculated at the MP2/(6-311+G(3f2g) level for Ti and the aug-cc-pvTz level for O and H) suggest that the oxygen partial charge should be somewhere between −0.65e and −0.74e. We have chosen a partial charge of −0.7e for O. The Ti partial charge was assigned a value of 1.4e to preserve the charge neutrality of the $TiO_2$ surfaces.

The nonbonded Ti−C, Ti−O, and Ti−H Lennard-Jones parameters shown in Table 2 were obtained by fitting the $TiO_5H_9/CH_3OCH_3$ binding energies from quantum chemistry calculations along the two paths shown in Figure 1. The exp-6 parameters for O−X, where X = O, C, or H, interactions were taken from the PEO force field[33] in order to decrease the total number of fitting parameters and make fitting more stable. The resulting fits to the $TiO_5H_9/CH_3OCH_3$ binding energies shown in Figure 1 are good. Figure 1 also indicates that the polarizable energy contributes substantially to the binding energy along path 1, suggesting that polarization should be included in the force field in some form.

Because MD simulations with the many-body polarizable terms are approximately 2−4 times more expensive than the MD simulations of identical systems with the force field containing only two-body interactions, it is desirable to develop a two-body force field for PEO/$TiO_2$ interactions that takes into account the many-body polarizable effects in a "mean-field" sense. Considering

**Table 2. Nonbonded Parameters for PEO/$TiO_2$ Interactions**

| atom pair | $A$ (kcal mol$^{-1}$ Å$^{-12}$) | | $C$ (kcal mol$^{-1}$ Å$^{-6}$) | $D$ (kcal mol$^{-1}$ Å$^{-4}$) |
|---|---|---|---|---|
| Ti−O | 97 622 | | 496.0 | 16 |
| Ti−C | 125 000 | | 645.0 | 18 |
| Ti−H | 88 630 | | 32.0 | 3 |
| atom pair | $A$ (kcal mol$^{-1}$) | $B$ (Å$^{-1}$) | $C$ (kcal mol$^{-1}$ Å$^{-6}$) | $D$ (kcal mol$^{-1}$ Å$^{-4}$) |
| $O_{Ti}$-O | 75 844.80000 | 4.063 | 396.89 | 0 |
| $O_{Ti}$-C | 33 702.40 | 3.57700 | 503.04 | 0 |
| $O_{Ti}$-H | 14 175.98 | 3.90150 | 103.95 | 0 |

only the lowest-order term in $r_{ij}$ in eq 2, the polarization energy between two charged atomic centers with dipolar polarizability is given by eq 3:

$$U^{\mathrm{POL}}(r_{ij}) = -\frac{332.07[q_i^2\,\alpha_j + q_j^2\alpha_i]}{2r_{ij}^4} = -\frac{D_{ij}}{r_{ij}^4} \quad (3)$$

where $\alpha_i$ and $\alpha_j$ are the atomic dipole polarizabilities. For the system with more than two charged polarizable atoms, eq 3 is not exact because it neglects interactions between the induced moments and induction from the other atoms; therefore, we call the $D$ parameter used in the condensed-phase simulations an effective $D$ parameter and determine it from condensed-phase simulations. The effective $D$ parameters for the condensed-phase simulations of PEO/$TiO_2$ were found by manually matching the PEO density profile near the $TiO_2$ surface from the short 100-ps MD simulation run with the many-body force field with the density profile from MD simulations with the two-body force field that included the effective $D$ parameters given in Table 2. Atomic partial charges for the effective two-body force field were taken from the many-body polarizable force field without modification. Following our previous work,[35] the $D_{ij}$ parameters are scaled to zero beyond the first coordination shell of atoms (3.5 Å) using a distance-dependent dielectric constant.

## III. MD Simulations Methodology and System Description

MD simulations of pure PEO and PEO sandwiched between two $TiO_2$ surfaces, as shown in Figure 2, have been performed. Ten PEO chains with the structure of $H-(CH_2-O-CH_2)_{54}-H$ were used in the simulations. A previously developed quantum chemistry-based two-body force field (FF-3 T-B)[33] was used to describe PEO−PEO interactions. Each $TiO_2$ surface comprises four atomic planes or layers of 336 Ti and 772 O from the (110) direction of an anatase crystal that is about 10 Å thick ($z$ dimension) and 27.4 and 29.5 Å in the $x$ and $y$ dimensions, respectively. The surfaces were frozen and placed symmetrically with respect to the middle of the box as shown in Figure 2.

All MD simulations were performed at 423 K using a modification of the Lucretius MD simulations package.[36] The system of PEO sandwiched between two $TiO_2$ surfaces was created by placing PEO in a box with a $z$ dimension of 230 Å between the surfaces. Then the box was shrunk in MD simulations for 3 ns to match the estimated experimental PEO density at 423 K in the middle of the PEO film and subsequently equilibrated in an NPT ensemble for 6 ns with the internal stress tensor component $P_{zz} = 0$ using the velocity Verlet algorithm with a 1-fs time step.[37] The 16-ns production runs were performed in an NVT ensemble with the box

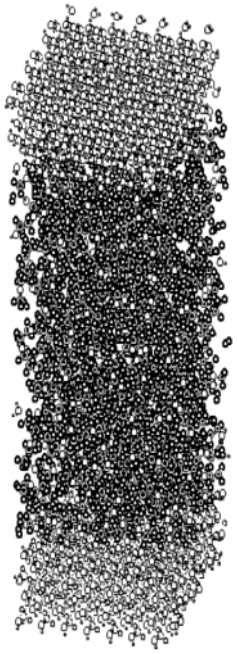

**Figure 2.** Snapshots of PEO sandwiched between two $TiO_2$ surfaces from MD simulations.

size corresponding to $P_{zz} = 0$, which was previously found in NPT simulations.

The distance between the $TiO_2$ surfaces through the periodic boundary was approximately 50 Å. A Nose−Hoover thermostat[38] and a barostat[39] were used to control the temperature and pressure, and bond lengths were constrained using the Shake algorithm.[40] The particle-mesh Ewald (PME) technique[41] was used to treat Coulomb interactions. A multiple time step reversible reference system propagator algorithm was employed,[42] with a 0.75-fs time step for bonding, bending, and torsional motions, a 1.5-fs time step for nonbonded interactions within a 6.5-Å sphere, and a 3.0-fs time step for both the nonbonded interactions between 6.5 and 10.0 Å and the reciprocal space part of the PME summation. The long-range correction to the cutoff of 10 Å of dispersion interactions was applied.

To investigate the effect of surface−polymer interactions on PEO structure and dynamics, two additional simulations were performed on PEO sandwiched between surfaces. In the first simulation, the $TiO_2$ charges were set to zero; this system is called a neutral surface system. In the second simulation, in addition to the $TiO_2$ charges being zero, the $TiO_2$/PEO dispersion parameters were set to zero, and the $TiO_2$/PEO repulsion parameters were made longer-range (Table 3), resulting in a soft repulsion between the surface and PEO. MD simulations of these systems were performed for 3 ns in NPT ensemble (equilibration) and 16 ns in NVT ensemble with the distance between two surfaces set

**Table 3. Nonbonded Parameters for PEO/SR-surface and PEO/Flat Surface Interactions**

PEO/SR Surface

| atom pair | $A$ (kcal mol$^{-1}$) | $B$ (Å$^{-1}$) | $C$ (kcal mol$^{-1}$ Å$^{-6}$) |
|---|---|---|---|
| Ti−O | 1416 | 1.96 | 0.0 |
| Ti−C | 674 | 1.70 | 0.0 |
| Ti−H | 282 | 1.80 | 0.0 |
| $O_{Ti}$−O | 674 | 1.70 | 0.0 |
| $O_{Ti}$−C | 674 | 1.70 | 0.0 |
| $O_{Ti}$−H | 282 | 1.80 | 0.0 |

PEO/Flat Surface

| atom type | $A'$ (kcal mol$^{-1}$ Å$^{-9}$) | $C$ (kcal mol$^{-1}$ Å$^{-3}$) |
|---|---|---|
| O | 633.3 | 31.83 |
| C | 633.3 | 17.65 |
| H | 633.3 | 6.59 |

to give a zero $P_{zz}$ component of the stress tensor and the PEO density in the middle of the box equal to the PEO bulk density.

MD simulations of PEO sandwiched between two flat (i.e., structureless) surfaces were also performed. The potential for the PEO/flat surface of the surface is given by eq 4:

$$U(z) = A_j' z^{-9} - C'_j z^{-6} \quad (4)$$

where $z$ is the distance between PEO atom $j$ (H, C, O) and the closest surface to the PEO atom. The $A'$ and $C$ parameters were optimized by matching the PEO density profile normal to the flat surface with the PEO density profile normal to the atomistic $TiO_2$ surfaces as closely as possible. The surface−X (X = O, C, H) repulsion parameters ($A_j'$) were constrained to have the same value, whereas the surface−X dispersion parameters ($C_j$) were constrained to be proportional to H−H, O−O, and C−C parameters, leaving only two adjustable parameters to govern the PEO−flat surface interactions: one for scaling the repulsion and one for scaling the dispersion parameters. The NPT MD simulations of PEO between flat surfaces were performed for 1.5 ns followed by the 7-ns NVT simulations at the distance between surfaces corresponding to the internal stress tensor component $P_{zz} = 0$ and the density of the middle of the PEO file equal to the bulk PEO density at the same temperature and 1 atm of pressure.

## IV. Influence of $TiO_2$ Surfaces on PEO Structure and Dynamic

**A. Structural Properties.** We begin our investigation of the influence of $TiO_2$ surfaces on PEO structure by analyzing the PEO density profile normal to $TiO_2$ surfaces, which is shown in Figure 3. The PEO density profile indicates strong PEO structuring up to approximately 10−14 Å, whereas the PEO density farther than 14 Å from the surface approaches the PEO melt density. The PEO at the $TiO_2$ surface is divided into three interfacial layers using the minima of the density profiles as shown in Figure 3 by the dotted lines. A snapshot of a part of the simulation box shown in Figure 3 represents the typical structure of PEO in the first interfacial layer. The PEO oxygen atoms approach closest the $TiO_2$ surface because of strong electrostatic interactions with the Ti atoms bearing a positive partial charge of 1.4e. Carbon atoms are positioned between two layers of the oxygen atoms as seen from the carbon and oxygen atom density profiles and from the simulation snapshot. Segments of the PEO chains in the first

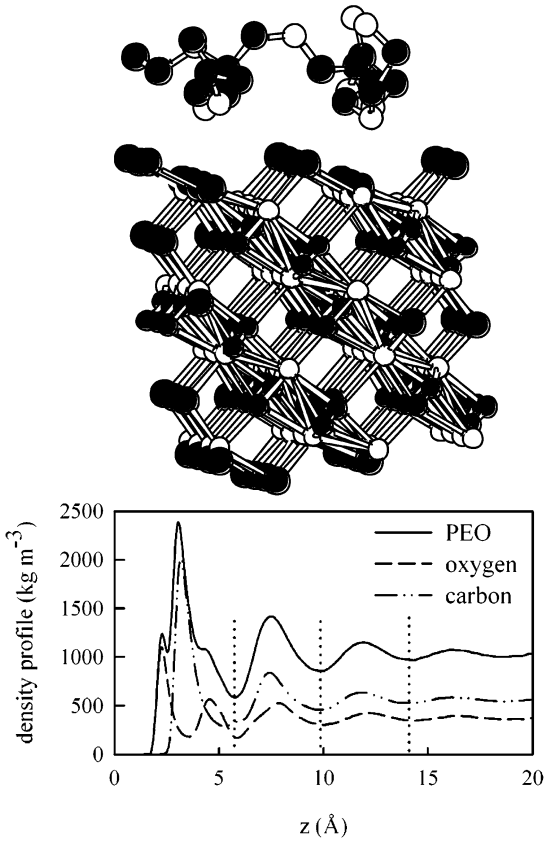


**Figure 3.** PEO density profile at $TiO_2$ surfaces. Vertical dashed lines indicate division into interfacial layers. A part of the simulation box is shown, with characteristic PEO structure in the first interfacial layer shown above the box.

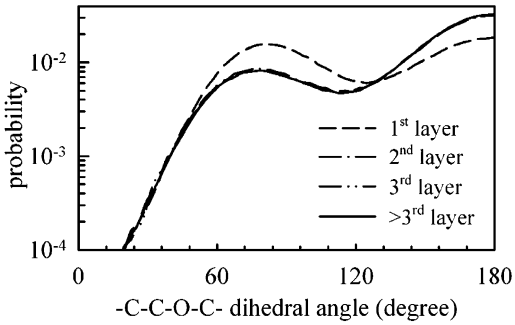


**Figure 4.** Probability distribution for the PEO C−O−C−C dihedral angles at $TiO_2$ surfaces.

interfacial layer have a preferential alignment on the surface as shown in the representative snapshot in Figure 3. The $Z$ component (normal to the surface) of the square of the radius of gyration decreases from about 120 Å$^2$ in the middle of the PEO film to less than 20 Å$^2$ in the first interfacial layer, indicating a flattening of the interfacial PEO in agreement with the previous simulations.[12,17,19]

PEO conformations are also perturbed by the presence of the $TiO_2$ surfaces. Figure 4 shows the C−C−O−C dihedral angle distribution for the PEO interfacial layers and PEO far from the interface. A given C−C−O−C dihedral is considered to be in a particular layer if the center of the C−O bond belongs to that layer. This criterion for assigning the dihedrals to the layers is used throughout this paper. Figure 4 illustrates that the influence of the $TiO_2$ surface on PEO conformations is very local (i.e., only PEO in the first interfacial layer

**Table 4. Parameters for C−O−C−C Dihedrals**[a]

| system | layer width (Å) | $t_{wait}/t_{wait}^{bulk}$ | $\tau_{TACF}/\tau_{TACF}^{bulk}$ | $\sigma^2/\sigma^{2\ bulk}$ | $\tau_{ISF}/\tau_{ISF}^{bulk}$ | $\tau_{ISF}^{Gauss}/\tau_{ISF}^{Gauss\ bulk}$ | $\tau_{ISF}/\tau_{ISF}^{Gauss}$ |
|---|---|---|---|---|---|---|---|
| PEO/$TiO_2$ | 4.2 | 1.2 | 5.1 | 11.3 | 490 | 32 | 14.1 |
| PEO/neutral surface | 5.3 | 1.0 | 1.0 | 1.5 | 1.9 | 1.2 | 1.7 |
| PEO/SR surface | 9.4−12.3 | 0.8 | 0.5 | 0.6 | 0.4 | 0.4 | 1.2 |
| PEO/flat surface | 6.7 | 1.0 | 1.0 | 1.5 | 0.9 | 0.9 | 1.2 |

[a] Mean waiting time for torsional transitions for C−O−C−C dihedrals ($t_{wait}$), torsional autocorrelation time for C−O−C−C dihedrals ($\tau_{TACF}$), dispersions of the distribution of torsional transition time for a C−O−C−C dihedral to undergo 10 torsional transitions ($\sigma^2$), structural relaxation times obtained from the decay of the intermediate incoherent structure factor ($\tau_{ISF}$), and structural relaxation times for Gaussian-distributed atom displacements $\tau_{ISF}^{Gauss}$ for PEO in the first interfacial layer relative to the corresponding times for bulk PEO calculated for the same layer width.

(∼4 to 5 Å) has conformations significantly different from those in bulk PEO, whereas PEO conformations in the second interfacial layer and farther away from the surface are essentially the same as in the bulk). Similar results are seen for the O−C−C−O dihedrals.

**B. Conformational Dynamics.** Polymer motion in the melt is intimately connected to its conformational dynamics and relaxation. Torsional transition is a fundamental step of conformational dynamics, whereas torsional relaxation described by the torsional autocorrelation function (TACF) is closely connected to polymer dielectric relaxation, viscosity, and $T_1$ spin−lattice relaxation.[43] The TACF is defined as

$$P(t) = \frac{\langle \cos \phi(t) \cos \phi(0) \rangle - \langle \cos \phi(0) \rangle^2}{\langle \cos \phi(0) \cos \phi(0) \rangle - \langle \cos \phi(0) \rangle^2} \qquad (5)$$

where $\phi(t)$ is the dihedral angle for a given dihedral of a particular type and the brackets denote the ensemble average over all dihedrals of that type.

To investigate the effect of $TiO_2$ surfaces on the conformational dynamics of PEO, we divided PEO into layers according to the minima of the density profile shown in Figure 3, as was done in the investigation of the distribution of dihedral angles shown in Figure 4. Because MD simulation trajectories were saved every 1 ps, the torsional transitions were considered to occur if the state of the dihedral changed over 1 ps. We found that the presence of the $TiO_2$ surface has only a minor effect on the intrinsic conformational dynamics, as reflected by the mean waiting time $t_{wait}$ between torsional transitions for PEO in the first interfacial layer being only 20% longer than that for bulk PEO as shown in Table 4. The effect of the $TiO_2$ surface on the mean waiting times for torsional transitions of the interfacial PEO beyond the first layer is negligible.

Torsional relaxation measured by the decay of the TACF, however, is affected more dramatically than expected from the mean waiting times between torsional transitions. The TACFs were calculated for each layer and plotted in Figure 5 versus the reduced time ($t^* = t/t_{wait}$), measured in units of the average number of torsional transitions. This Figure allows us to examine the difference between torsional relaxation probed through the TACF and intrinsic conformational dynamics measured by $t_{wait}$. A given dihedral was included in the TACF statistics as long as it is continuously present in the layer. Because of the finite width of the first three layers (∼4.2 Å), a significant number of dihedrals exited the layer, reducing the statistics at long times. It is reasonable to assume that the "fast" dihedrals exited the finite layer sooner than the "slow" dihedrals, resulting in a slightly slower decay of the TACF for PEO belonging to the finite layer compared to the decay of the PEO TACF calculated for the much larger layer as

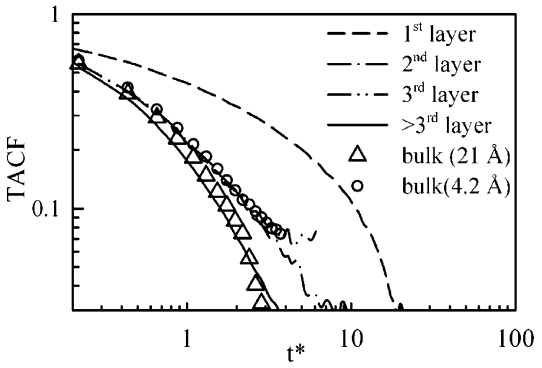


**Figure 5.** PEO C−O−C−C TACFs at $TiO_2$ surfaces and in bulk PEO.

shown in Figure 5. Therefore, one should compare TACF calculated for the interfacial PEO in finite layers to those for the bulk PEO divided into layers of the same size. The decay of the TACFs for PEO in the second and third interfacial layers and beyond is similar to that of bulk PEO, indicating that the influence of $TiO_2$ surfaces on PEO conformational relaxation is very local and is limited to the first interfacial PEO layer that extends only 4 to 5 Å from the $TiO_2$ surface, at least at the temperature investigated (423 K). The decay of the TACF in the first interfacial layer is dramatically slower than that for bulk PEO, which is indicative of the decreased efficacy of conformational transitions on polymer conformational relaxation previously observed in simulations of polymer melts[44] and polymer electrolytes.[45] To obtain a quantitative measure of the slowing down of the conformational relaxation of the interfacial PEO relative to that in bulk PEO, the torsional autocorrelation times $\tau_{TACF}$ are calculated as time integrals of the stretched exponential $\exp[-(t/\tau)^{\beta}]$ fits of the TACF for decay up to 0.1. The ratio of the torsional autocorrelation time of interfacial PEO to that of the bulk PEO is 5.1 (Table 4) compared to the ratio of mean waiting times $t_{wait}/t_{wait}^{bulk} = 1.2$, indicating that the influence of $TiO_2$ surfaces on interfacial PEO conformational relaxation (TACF) is 4.25 times larger than its the influence on mean waiting times between torsional transitions.

To understand the reason for the decreased efficacy of conformational transitions on conformational relaxation, we analyzed the distribution of torsional transitions. Figure 6a shows the probability density for 10 torsional transitions to occur at reduced time $t^* = t/t_{wait}$ in bulk PEO layers of 21 and 4.2 Å. The dependence of the distribution of torsional transitions on the layer size is due to torsions leaving the layer before they can contribute to the spectrum of torsional transition times at long time. To correct effectively for the effect of the finite layer size, the distribution of PEO torsional

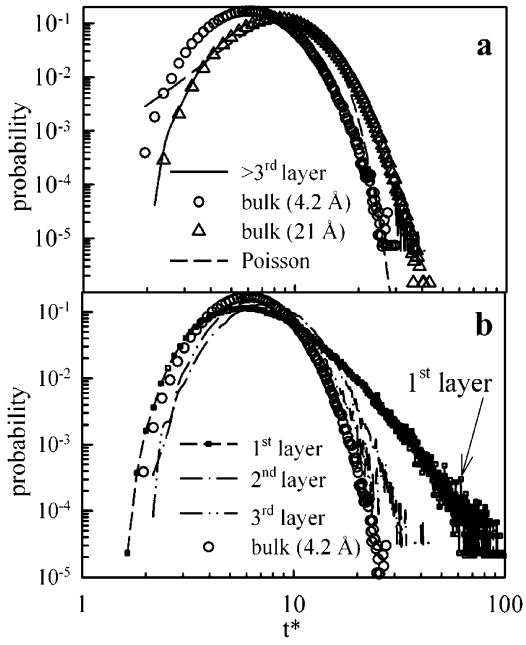


**Figure 6.** Probability distribution for C−O−C−C dihedrals to undergo 10 torsional transitions vs reduced time ($t^*$) for bulk PEO layers of 4.2 and 21 Å and interfacial PEO at $TiO_2$ surfaces.

transitions for interfacial layers is compared to the distributions of bulk PEO calculated for the same layer thicknesses. The PEO beyond the third interfacial layer has the distribution of torsional transitions identical to that of bulk PEO of the same layer thickness of 21 Å and is only slightly wider than the Poisson distribution corresponding to the random (uncorrelated) events of torsional transitions. Weak correlations between torsional transitions are expected at the temperature, 423 K, which is much higher than the glass-transition temperature of PEO, ~213 K.[43,44] The distributions of torsional transitions for the interfacial PEO in the second and third layers shown in Figure 6b are similar to those of bulk PEO. An examination of the distribution of torsional transitions for the first interfacial layer of PEO reveals a long time tail due to the increased number of "slow" dihedrals with long waiting times between torsional transitions and some increase in the population of the "fast" dihedrals with short waiting times between transitions compared to that for the bulk PEO. Thus, the distribution of torsional transitions of interfacial PEO is much wider than that of bulk PEO, and the dispersion of conformational transitions of interfacial PEO is an order of magnitude larger than the dispersion of torsional transitions of bulk PEO, as seen from Table 4. The mean waiting time between torsional transitions for PEO next to the $TiO_2$ surface compared to that for the bulk, however, remained basically unchanged ($t_{wait}/t_{wait}^{bulk} = 1.2$) despite the dramatic increase in the dispersion of torsional transitions.

Our previous simulations[44] used a simple two-state model and demonstrated that the increased dispersion of transitions with the average transition rate constant leads to a slower relaxation. The behavior of the distribution of torsional transitions and TACF for the interfacial PEO compared to that for bulk PEO closely resembles the results of this model. Indeed, the increased number of fast dihedrals in interfacial PEO does not significantly influence the decays of TACF because

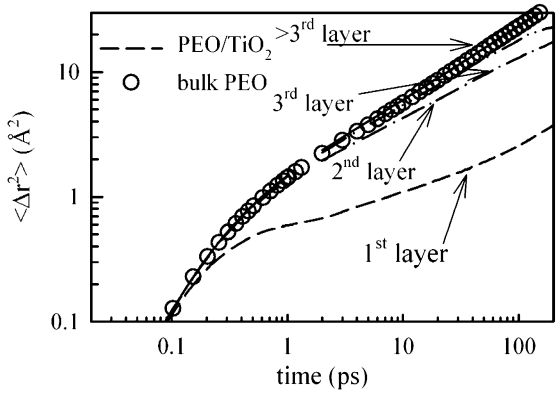


**Figure 7.** Mean-square displacements for interfacial PEO backbone atoms at $TiO_2$ surfaces and bulk PEO.

such fast dihedrals characterized by extremely short waiting times between transitions exhibit self-correlated transitions resulting in immediate or near-immediate back jumps. Dihedrals undergoing back jumps are rather ineffective in polymer relaxation because polymer relaxation requires each dihedral to visit *all* conformational states with average probability. Slow dihedrals, however, are very effective in hindering the relaxation of TACF. Therefore, the slowing down of PEO relaxation because of an increased number of slow dihedrals in interfacial PEO compared to the number in bulk PEO prevails over the insignificant speed up of PEO relaxation due to an increased number of fast dihedrals. Similar behavior is seen for polymers approaching the glass-transition temperature.[43]

**C. Translational Dynamics.** To examine the influence of $TiO_2$ surfaces on PEO translational dynamics, the mean-square displacements (MSD) of the PEO backbone atoms in a plane parallel to the $TiO_2$ surfaces (e.g., $x-y$ plane) were calculated. Mean-square ($x$, $y$) displacements of PEO backbone atoms calculated for each interfacial layer are shown in Figure 7. This Figure demonstrates that PEO backbone atoms in the first layer adjacent to $TiO_2$ surfaces were significantly slower than those in bulk PEO. The PEO dynamics in the second layer, however, is perturbed significantly less than the PEO dynamics in the first layer, whereas the MSD of PEO atoms in the third layer and beyond is essentially the same as in the bulk, consistent with the behavior of the PEO TACFs.

Molecular dynamics simulations allowed us to investigate in detail the effect of solid interfaces on polymer dynamics by considering the structural relaxation of PEO backbone atoms in addition to MSD. Quasielastic neutron scattering and neutron spin−echo experiments also probe polymer structural relaxation; however, these experimental methods do not allow us to measure mean-square displacement directly; instead, an incoherent structure factor (ISF) in the frequency domain $S(Q, \omega)$ or in time domain $I(Q, t)$ is measured in such experiments probing local polymer dynamics. Because of the similarity in the decay of PEO coherent and incoherent intermediate structure factors[46] far from the glass-transition temperature, we assume that PEO structural relaxation is reflected reasonably by the incoherent (or self-) scattering function. The decay of ISF at the position of the first peak of the PEO structure factor[47] occurring at $Q = 1.5$ Å$^{-1}$ can be used to approximate PEO structural relaxation. A component of the ISF describing polymer motion in the $x-y$ plane is given by

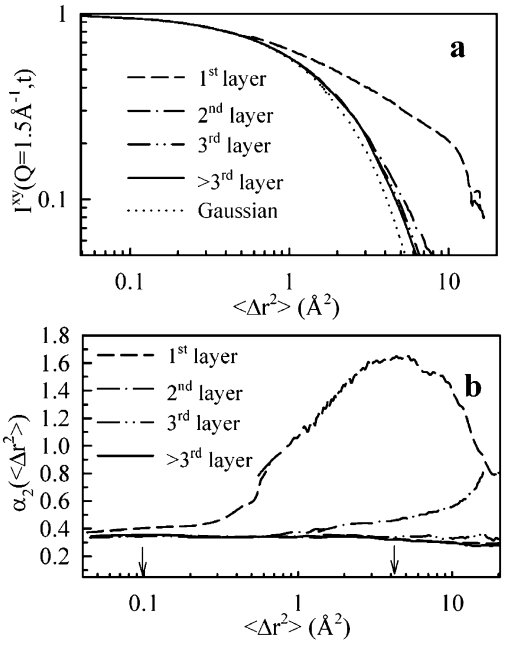


**Figure 8.** Incoherent intermediate structure factor (a) and non-Gaussian parameter (b) for interfacial PEO near $TiO_2$ surfaces.

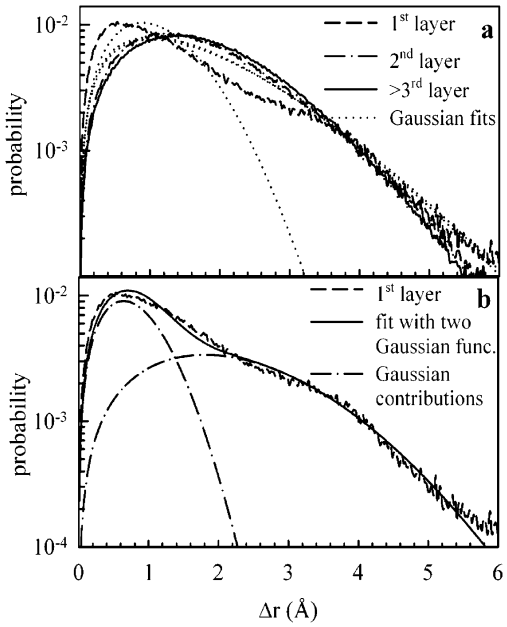


**Figure 9.** Distribution of PEO backbone atom displacements calculated for times that $\langle \Delta r^2(t) \rangle = 3.5$ Å$^2$ for interfacial PEO at $TiO_2$ surfaces. Gaussian fits to the distributions are also shown.

eq 6:

$$I^{x-y}{}_{\mathrm{inc}}(Q, t) = \langle \cos(\Delta \mathbf{r}_{x-y}(t)\mathbf{Q}) \rangle \qquad (6)$$

where $\Delta \mathbf{r}_{x-y}(t)$ is the atom displacement vector after time $t$ in the $x-y$ plane, $\mathbf{Q}$ is the momentum transfer vector, and $\langle\ \rangle$ denotes an average over all time origins for atoms with a significant incoherent cross section and an average over all possible directions of the $\mathbf{Q}$ vector in the plane. One hundred twenty directions of the $\mathbf{Q}$ vector were used to average the ISF.

If polymer atom displacements are Gaussian, then the ISF is represented by eq 7:

$$I^{\mathrm{Gauss}}{}_{\mathrm{inc}}(Q, t) = \exp\left(\frac{-Q^2 \langle \Delta r^2{}_{x-y}(t) \rangle}{4}\right) \qquad (7)$$

For Gaussian mean-square displacements, $I^{\mathrm{Gauss}}{}_{\mathrm{inc}}(Q, t)$ depends only on the MSD for a given $\mathbf{Q}$ vector and can be readily backed out from the experimental measurements. $I^{x-y}{}_{\mathrm{inc}}(Q, t)$ was calculated for each layer of PEO adjacent to $TiO_2$ surfaces and for bulk PEO. $I^{x-y}{}_{\mathrm{inc}}(Q, t)$ plotted verses PEO backbone mean-square displacements $\langle \Delta r^2{}_{x-y}(t) \rangle$ are shown in Figure 8a. This Figure indicates that atom displacements in bulk PEO and PEO in the third layer and beyond it in the PEO/$TiO_2$ system only slightly deviate from Gaussian behavior, whereas a more significant deviation from Gaussian behavior is observed with PEO getting closer to the $TiO_2$ surface (e.g., in the second and especially the first interfacial layer). The non-Gaussian behavior of PEO mean-square displacements results in a dramatically slower decay of $I^{x-y}{}_{\mathrm{inc}}(Q, t)$ for the first interfacial layer than expected from MSD and eq 7 as demonstrated by Figure 8a. We define the structural relaxation time $\tau_{\mathrm{ISF}}$ and structural relaxation time assuming a Gaussian distribution of atom displacements $\tau_{\mathrm{ISF}}{}^{\mathrm{Gauss}}$ as time integrals of the stretched exponential fits of $I_{\mathrm{inc}}(Q, t)$ and $I^{\mathrm{Gauss}}{}_{\mathrm{inc}}(Q, t)$ from 1 up to a 0.1 decay and for $t > 1$ ps to exclude the ballistic regime. The effect of the $TiO_2$ surface on $\tau_{\mathrm{ISF}}$ for interfacial PEO is more than an order of magnitude larger than the effect on $\tau_{\mathrm{ISF}}{}^{\mathrm{Gauss}}$, as seen from Table 4. This is a significant fact, indicating that standard models of polymer behavior assuming Gaussian displacements should not be applied to the analysis of polymer dynamics in nanocomposites with nanoparticles such as $TiO_2$ or that the non-Gaussian correction should be included in the model.

The leading-term correction to the ISF for non-Gaussian behavior is given by eqs 8 and 9:

$$I^{x-y}{}_{\mathrm{inc}}(Q, t) = I^{\mathrm{Gauss}}{}_{\mathrm{inc}}(Q, t) * \left[1 + 0.5 * \left(\frac{Q^2 \Delta r^2{}_{x-y}(t)}{6}\right) \alpha_2(t) + \ldots\right] \qquad (8)$$

$$\alpha_2(t) = \frac{3\langle \Delta r^4{}_{x-y}(t) \rangle}{5\langle \Delta r^2{}_{x-y}(t) \rangle^2} - 1 \qquad (9)$$

where $\alpha^2(t)$ is the non-Gaussian parameter. The behavior of the non-Gaussian parameter for interfacial and bulk PEO is shown in Figure 8b. The non-Gaussian parameter for the first interfacial layer is about 6 times larger than that for bulk PEO and the third interfacial PEO layer, consistent with ISF behavior versus MSD shown in Figure 8a. A broad maximum in the non-Gaussian parameter for bulk PEO is observed at ~0.1−0.3 Å$^2$, corresponding to the displacements at which PEO backbone atoms start leaving the weak cage formed by its neighbors. The maximum in the non-Gaussian parameter for the first interfacial PEO layer occurs at much larger mean-square displacements of ~4.2 Å$^2$ and thus cannot be associated with polymer caging by the neighboring polymer. To understand the underlying physical mechanisms leading to the increase in the non-Gaussian parameter for the interfacial polymer, the distribution of the displacements is calculated for times corresponding to the maximum in the non-Gaussian parameter (e.g., $\langle \Delta r^2(t) \rangle = 4.2$ Å$^2$) and is shown in Figure 9. The displacement distributions for

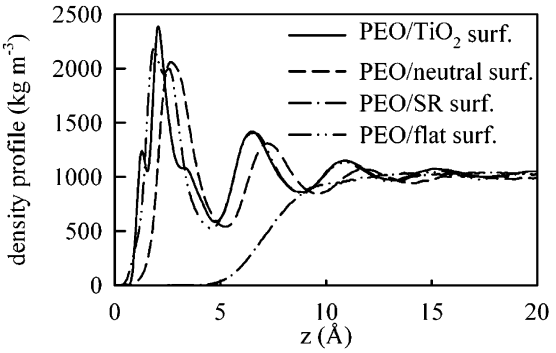


**Figure 10.** PEO density profile vs distance from the surfaces (z).

the second and third interfacial layer and bulk PEO are essentially Gaussian, in agreement with the ISF behavior shown in Figure 8a. The displacement distribution for PEO in the first interfacial layer exhibits a pronounced shoulder that cannot be described by a single Gaussian function; however, it can be reasonably described by two Gaussian functions with the most probable displacements at 0.64 and 1.8 Å, as shown in Figure 9b. The first Gaussian corresponds to Gaussian vibrations of PEO backbone atoms trapped in potential wells on the surface of $TiO_2$, whereas the second Gaussian corresponds to the PEO backbone atoms jumping the most probable distance of 1.8 Å from one potential well to an adjacent well located approximately one Ti−O distance away. The picture of PEO backbone atoms vibrating in potential wells on the $TiO_2$ surface and jumping to the closest potential well emerges. We conclude that the PEO backbone atom displacements in the first interfacial layer are highly non-Gaussian and are intimately related to the structure of the $TiO_2$ surface rather than bulk PEO.

## V. Effect of Surface Structure on PEO Dynamics

We have demonstrated that the PEO interfacial dynamics near $TiO_2$ is correlated with the surface structure. Surface structure was also found to influence the interfacial dynamics and glass-transition temperature in previous studies[13,21] of bead−spring models of polymers, whereas McCoy et al.[48] hypothesized that the inhomogeneous density profile can account for the shift in the glass-transition temperature upon polymer confinement. We wish to separate the effect of inhomogeneous and increased density from the effect of surface structure on polymer dynamics by comparing interfacial polymer dynamics from MD simulations of PEO between $TiO_2$ atomic surfaces and two flat (structureless) surfaces that have very similar density profiles. Figure 10 shows the PEO density profile for the PEO/flat surface system fitted to the density profile of the PEO/$TiO_2$ system. Interfacial PEO in the PEO/flat surface system is divided into three layers according to the density profile, as was done for the PEO/$TiO_2$ system. Figure 11 shows that conformational distributions for the interfacial C−O−C−C dihedrals near flat surfaces are essentially identical to those for bulk PEO, suggesting that significant perturbations in the PEO density profile do not cause any noticeable perturbations of the PEO conformations.

The TACFs for the first interfacial layer in the PEO/flat surface system are compared to those for the PEO/$TiO_2$ system in Figure 12. This Figure demonstrates

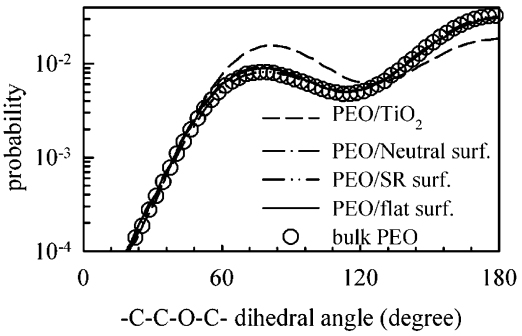


**Figure 11.** Probability distribution for the C−O−C−C dihedrals of the interfacial and bulk PEO.

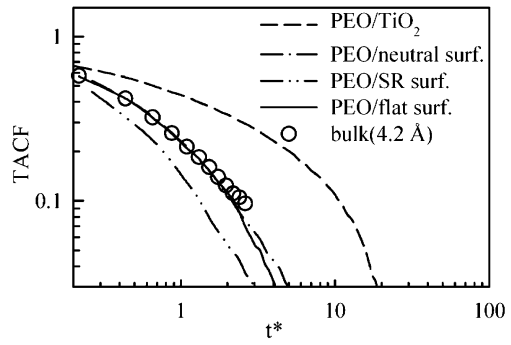


**Figure 12.** TACFs for the C−O−C−C dihedrals for the interfacial and bulk PEO.

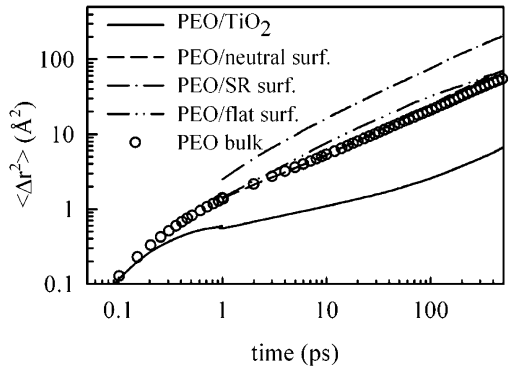


**Figure 13.** Mean-square displacements for the interfacial PEO backbone atoms at bulk PEO.

that despite the similarity of PEO density profiles next to the flat surface and $TiO_2$, the TACFs of the interfacial PEO next to $TiO_2$ and the flat surface are quite different. In fact, the decay of the TACF of interfacial PEO next to the flat surface is almost identical to that of the bulk PEO, suggesting that flat surfaces have no effect on conformational relaxation, unlike that seen for PEO/$TiO_2$ atomic surface systems. The PEO torsional transition times, backbone mean-square displacements, and non-Gaussian parameters shown in Table 4 and Figures 13 and 14, respectively, also demonstrate that the PEO structural and conformational relaxations near flat surfaces are similar to those of bulk PEO and quite different from those for the PEO/$TiO_2$ system, suggesting that the surface structure rather than the density profile is the primary factor influencing the interfacial PEO relaxation at $TiO_2$ surfaces.

## VI. Influence of PEO−Surface Interaction on PEO Structure and Dynamics

We investigated dynamic and structural properties of the technologically important PEO/$TiO_2$ system.

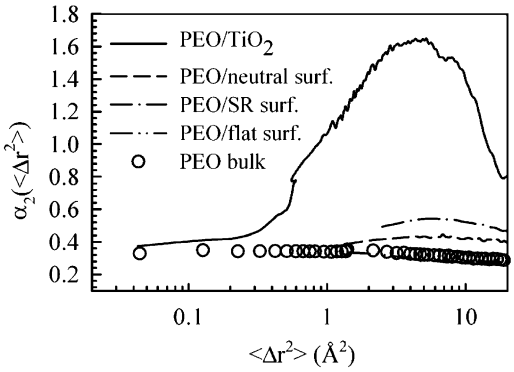


**Figure 14.** Non-Gaussian parameter for the interfacial PEO at surfaces.

Previous MD simulations[15−17] of the bead−spring models indicated that polymer dynamics and viscosity can be significantly decreased if polymer/surface interactions are strongly attractive and that polymer dynamics can be increased if polymer/surface interactions are repulsive. It is interesting to understand the extent to which the PEO/$TiO_2$ Coulomb interactions influence PEO dynamics. This is achieved by simulating the PEO/$TiO_2$ system with $TiO_2$ charges set to zero. This system is called the PEO/neutral surface system. We investigated the possibility of speeding up PEO dynamics at the surfaces by simulating PEO sandwiched between two surfaces with the $TiO_2$ structure, but soft repulsion (SR) interaction between the surface atoms and PEO as seeding up the interfacial PEO dynamics is desirable in battery and other applications of PEO.

Density profiles of PEO near the neutral surface and SR surface are shown in Figure 10. The peak in the PEO density profile from the neutral surface is less pronounced and shifted farther away from the surface than that seen for PEO/$TiO_2$. The PEO density profile near the SR surfaces does not exhibit any structuring peaks; instead, it shows a region of about 10 Å with density below the PEO bulk density. All profiles converge to the PEO bulk density 12−15 Å from the surface. Distributions of the torsional C−O−C−C angles for the interfacial PEO at the neutral and SR surfaces, shown in Figure 11, are essentially identical to those for bulk PEO, indicating that changes in PEO conformations are insignificant for the neutral and SR surfaces compared to those observed for PEO/$TiO_2$.

The TACFs for all surface types are shown in Figure 12. The torsional autocorrelation times $\tau_{TACF}$, mean waiting times between torsional transitions $t_{wait}$, dispersions of torsional transitions $\sigma^2$, and structural relaxation times for interfacial PEO at neutral and SR surfaces relative to those for bulk PEO are given in Table 4. All ratios of interfacial PEO values near neutral surfaces to those of bulk PEO are close to unity, indicating little influence of neutral surfaces on PEO interfacial dynamics. Interfacial PEO at the SR surfaces exhibits a 50% faster decay of TACF, whereas the mean waiting times between torsional transitions are decreased only by 20%. A decrease in the dispersion of torsional transitions in the interfacial PEO near SR surfaces is responsible for the additional (from 20 to 50%) speed up of the interfacial PEO dynamics near SR surfaces.

The interfacial PEO near neutral surfaces exhibits PEO bulklike MSDs as shown in Figure 13, whereas the analysis of the MSDs for the interfacial PEO near the SR surface indicates a significant speed up of PEO relaxation as seen in Figure 13 and Table 4. The non-Gaussian $\alpha^2$ parameter for interfacial PEO near SR and neutral surfaces is small and only slightly higher than that for bulk PEO as seen in Figure 14, indicating that the models assuming polymer Gaussian behavior would work reasonably well for such systems far from the glass-transition temperature.

## VII. Conclusions

MD simulations of PEO at $TiO_2$ surfaces revealed significantly perturbed PEO structure (density profile and conformations) and hindered PEO conformational and structural relaxations within 5−10 Å of the $TiO_2$ surface as compared to those for bulk PEO. The diminished PEO conformational relaxation at $TiO_2$ surfaces compared to that for bulk PEO was primarily due to the dramatically increased heterogeneity of torsional transitions and cannot be attributed to the changes in waiting times between torsional transitions. The slower interfacial PEO structural relaxation as measured by the ISF is attributed to both the slowing down of intrinsic PEO translational dynamics and the increased non-Gaussian behavior of the PEO atom displacement. The distribution of atom displacements for the interfacial PEO at $TiO_2$ is highly non-Gaussian and bimodal, giving rise to the picture of PEO backbone atoms vibrating in potential wells on the $TiO_2$ surface and jumping to the closest potential well, thus indicating that the structure of the $TiO_2$ surface is intimately related to interfacial polymer dynamics. MD simulations of PEO between flat (structureless) surfaces with interactions modified to match PEO density profiles to those of the PEO between the atomistic $TiO_2$ surfaces revealed no significant differences between the structural and conformation relaxation of the interfacial PEO and the PEO bulk, indicating that the PEO density near surfaces has only a minor influence on interfacial PEO dynamics and that perturbations of the interfacial PEO dynamics near $TiO_2$ surfaces are largely due to the atomistic structure of the $TiO_2$ surfaces and not the densification of interfacial PEO.

Eliminating the Coulomb interactions between PEO and $TiO_2$ significantly increased the structural and conformational relaxation times of the interfacial PEO, demonstrating that these interactions are responsible for the slowing of PEO dynamics. Moreover, the relaxation of the interfacial PEO in the PEO/neutral surface system is similar to that in bulk PEO, suggesting that the surface with the $TiO_2$ structure and no Coulomb interaction with PEO does not significantly perturb the PEO dynamics. The reduction of the repulsive interaction between the neutral surface and PEO further facilitated the relaxation of the interfacial PEO, in agreement with the results of polymer film simulations in vacuum.

We conclude that in addition to such intrinsic parameters as torsional potentials, polymer−surface interactions and surface structure (at least for attractive polymer−surface interactions) are two fundamental factors that determine interfacial polymer relaxations in PEO/$TiO_2$ nanocomposites.

**Acknowledgment.** We are indebted to NASA (grant NAG3 2624) for financial support. We also thank our collaborators Larry Curtiss, John Kerr, David Price,

Marie-Louise Saboungi, Jean-Mark Zanotti, James Smith, and Dmitry Bedrov.

## References and Notes


(1) Tsagaropoulos, S.; Eisenberg, A. *Macromolecules* **1995**, *28*, 396.
(2) Tsagaropoulos, G.; Eisenberg, A. *Macromolecules* **1995**, *28*, 6067.
(3) Cho, Y.-K.; Watanabe, H.; Granick, *J. Chem. Phys.* **1999**, *110*, 9688.
(4) Gagliardi, S.; Arrighi, V.; Ferguson, R.; Telling, M. T. F. *Physica B* **2001**, *301*, 110.
(5) Li, M.; Chen. Q. *Polymer* **2003**, *44*, 2793.
(6) Cochrane, H.; Lin, C. S. *Rubber Chem. Technol.* **1993**, *66*, 48.
(7) Sternstein, S. S.; Zhu, Ai-Jun *Macromolecules* **2002**, *35*, 7262−7273
(8) Shukla, N.; Gellman, A. J. *Langmuir* **2000**, *16*, 6562.
(9) Croce, F.; Appetecchi, G. B.; Persi, L.; Scrosati, B. *Nature* **1998**, *394*, 456−458.
(10) Almeida, E. *Ind. Eng. Chem. Res.* **2001**, *40*, 15.
(11) Walls, H. J.; Zhou, J.; Yerian, J.. A.; Fedkiw, P. S.; Khan, S. A.; Stowe, M. K.; Baker, G. L. *J. Power Sources* **2000**, *89*, 156.
(12) Yoon, D. Y.; Vacatello, M.; Smith, G. D. In *Monte Carlo and Molecular Dynamics Simulations in Polymer Science*; Binder, K., Ed.; Oxford University Press: New York, 1995.
(13) Scheidler, P.; Kob, W.; Binder, K. *Europhys. Lett.* **2002**, *59*, 701
(14) Aoyagi, T.; Takimoto, J.; Doi, M. *J. Chem. Phys.* **2001**, *115*, 552.
(15) Smith, G. D.; Bedrov, D.; Li, L.; Byutner, O. *J. Chem. Phys.* **2002**, *117*, 9478.
(16) Starr, F. W.; Schrøder, T. B.; Glotzer, S. C. *Macromolecules* **2002**, *35*, 4481.
(17) Baschnagel, J.; Binder, K.; Nilchev, A. In *Polymer Surfaces, Interfaces and Thin Films*; Karim, A., Kumar, S., Eds.; World Scientific Publishing: Singapore, 2000.
(18) Vacatello, M. *Macromolecules* **2001**, *34*, 1946−1952
(19) Mischler, C.; Baschnagel, J.; Dasgupta, S.; Binder, K. *Polymer* **2002**, *43*, 467.
(20) Vacatello, M, *Macromolecules* **2002**, *35*, 8191−8193
(21) Smith, G. D.; Bedrov, D.; Borodin, O. *Phys. Rev. Lett.* **2003**, *90*, 226103.
(22) Croce, F.; Curini, R.; Martinelli, A.; Persi, L.; Ronci, F.; Scrosati, B.; Caminiti, R. *J. Phys. Chem. B* **1999**, *103*, 10632−10638.
(23) Appetecchi, G. B.; Croce, F.; Dautzenberg, G.; Matragostino, M.; Ronc, F.; Scrosati, B.; Soavi, F.; Zanelli, F.; Alessandrini, F.; Prosini, P. P. *J. Electrochem. Soc.* **1998**, *145*, 4126−4132.
(24) Appetecchi, G. B.; Croce, F.; Mastragostino, M.; Scrosati, B.; Soavi, F.; Zaneli, F. *J. Electrochem. Soc.* **1998**, *145*, 4133−4135.
(25) Capiglia, C.; Mustarelli, P.; Quartarone, E.; Tomasi, C.; Magistris, A. *Solid State Ionics* **1999**, *118*, 73−79.
(26) Scrosati, B.; Croce, F.; Persi, L. *J. Electrochem. Soc.* **2000**, *147*, 1718−1721.
(27) Kumar, B.; Scanlon, L. G. *Solid State Ionics* **1999**, *124*, 239−254.
(28) Frisch, M. J.; Trucks, G. W.; Schlegel, H. B.; Scuseria, G. E.; Robb, M. A.; Cheeseman, J. R.; Zakrzewski, V. G.; Montgomery, J. A., Jr.; Stratmann, R. E.; Burant, J. C.; Dapprich, S.; Millam, J. M.; Daniels, A. D.; Kudin, K. N.; Strain, M. C.; Farkas, O.; Tomasi, J.; Barone, V.; Cossi, M.; Cammi, R.; Mennucci, B.; Pomelli, C.; Adamo, C.; Clifford, S.; Ochterski, J.; Petersson, G. A.; Ayala, P. Y.; Cui, Q.; Morokuma, K.; Malick, D. K.; Rabuck, A. D.; Raghavachari, K.; Foresman, J. B.; Cioslowski, J.; Ortiz, J. V.; Stefanov, B. B.; Liu, G.; Liashenko, A.; Piskorz, P.; Komaromi, I.; Gomperts, R.; Martin, R. L.; Fox, D. J.; Keith, T.; Al-Laham, M. A.; Peng, C. Y.; Nanayakkara, A.; Gonzalez, C.; Challacombe, M.; Gill, P. M. W.; Johnson, B. G.; Chen, W.; Wong, M. W.; Andres, J. L.; Head-Gordon, M.; Replogle, E. S.; Pople, J. A. *Gaussian 98*, revision A.7; Gaussian, Inc.: Pittsburgh, PA, 1998.
(29) van Duijneveldt, F. B.; van Duijneveldt-van de Rijdt, J. G. C. M.; van Lenthe, J. H. *Chem. Rev.* **1994**, *94*, 1873.
(30) Woon, D. E.; Dunning, T. H., Jr. *J. Chem. Phys.* **1993**, *98*, 1358.
(31) Ruocco, G.; Sampoli, M. *Mol. Phys.* **1994**, *82*, 875.
(32) Stone, A. J. *The Theory of Intermolecular Forces*; Oxford University Press: New York, 1996.
(33) Borodin, O.; Smith, G. D. *J. Phys. Chem. B* **2003**, *107*, 6801.
(34) Breneman, C. M.; Wiberg, K. B. *J. Comput. Chem.* **1990**, *11*, 361.
(35) Borodin, O.; Smith, G. D.; Douglas, R. *J. Phys. Chem. B* **2003**, *107*, 6824.
(36) *Lucretius*; www.che.utah.edu/∼gdsmith.
(37) Allen, M. P.; Tildesley, D. J. *Computer Simulation of Liquids*; Oxford University Press: New York, 1987.
(38) Nose, S. In *Computer Simulation in Materials Science*; Meyer, M., Pontikis, V., Eds.; Kluwer Academic Publishers: Dordrecht, The Netherlands, 1991; p 21.
(39) Martyna, G. J.; Tuckerman, M.; Tobias, D. J.; Klein, M. L. *Mol. Phys.* **1996**, *87*, 1117.
(40) Ryckaert, J. P.; Ciccotti, G.; Berendsen, H. J. C. *J. Comput. Phys.* **1977**, *23*, 327.
(41) Deserno, M.; Holm, C. *J. Chem. Phys.* **1998**, *109*, 7678.
(42) Martyna, G. J.; Tuckerman, M.; Tobias, D. J.; Klein, M. L. *Mol. Phys.* **1996**, *87*, 1117
(43) Smith, G. D.; Borodin, O.; Paul, W. *J. Chem. Phys.* **2002**, *117*, 10350.
(44) Smith, G. D.; Borodin, O.; Bedrov, D.; Paul, W.; Qiu, X. H.; Ediger, M. D. *Macromolecules* **2001**, *34*, 5192.
(45) Borodin, O.; Smith, G. D. *Macromolecules* **2000**, *33*, 2273.
(46) Saboungi, M.-L.; Price, D. L.; Mao, G.; Fernandez-Perea, R.; Borodin, O.; Smith, G. D.; Armand, M.; Howells, W. S. *Solid State Ionics* **2002**, *147*, 225−236.
(47) Borodin, O.; Douglas, R.; Smith, G. D.; Trouw, F.; Petrucci, S. *J. Phys. Chem. B* **2003**, *107*, 6813.
(48) McCoy, J. D.; Curro, J. G. *J. Chem. Phys.* **2002**, *116*, 9154.


MA0346005